An Iron(II) Spin-Crossover Metallacycle from a Back-to-Back *bis*-[Dipyrazolylpyridine]

Laurence J. Kershaw Cook[a], Julie Fisher[a], Lindsey P. Harding[b] and Malcolm A. Halcrow*[a]

[a]*School of Chemistry, University of Leeds, Woodhouse Lane, Leeds, UK LS2 9JT. E-mail: m.a.halcrow@leeds.ac.uk*
[b]*Department of Chemical and Biological Sciences, University of Huddersfield, Huddersfield, UK HD1 3DH.*

Supporting Information

Figure S1. Alternative view of the unique molecule in the crystal structure of bppSSbpp, showing the atom numbering scheme employed.

Figure S2. Packing diagram of bppSSbpp.

Figure S3. Variable temperature magnetic susceptibility data for the salts of $[Fe(bppSH)_2]^{2+}$: **1[BF$_4$]$_2$** and **1[ClO$_4$]$_2$**.

Figure S4. Room temperature X-ray powder diffraction data for **1[BF$_4$]$_2$** and **1[ClO$_4$]$_2$**.

Figure S5. First derivative of the $\chi_M T$ *vs T* curve for **1[ClO$_4$]$_2$** in the vicinity of its abrupt spin-transition, showing the splitting of the transition into two closely spaced components.

Figure S6. DSC analysis of **1[ClO$_4$]$_2$**.

Figure S7. Room temperature X-ray powder diffraction data for bppSSbpp, and the amorphous complexes **2[BF$_4$]$_2$**, **2[ClO$_4$]$_2$** and **3[BF$_4$]$_2$**.

Figure S8. ^{1}H NMR spectrum of **2[BF$_4$]$_2$** in CD_3NO_2.

Figure S9. ^{1}H NMR spectrum of **3[BF$_4$]$_2$** in CD_3NO_2.

Figure S10. DOSY spectrum of the bppSSbpp ligand in CD_3NO_2.

Figure S11. DOSY spectrum of **3[BF$_4$]$_2$** in CD_3NO_2.

Table S1 Relative intensities and assignments of the principle peaks in the ES mass spectra of the $[\{M(\mu\text{-bppSSbpp})\}_n]^{2n+}$ assemblies.

Figure S12. Electrospray mass spectrum of **2[BF$_4$]$_2$** from $MeNO_2$ solution.

Figure S13. Electrospray mass spectrum of **2[ClO$_4$]$_2$** from $MeNO_2$ solution.

Figure S14. Electrospray mass spectrum of **3[BF$_4$]$_2$** from $MeNO_2$ solution.

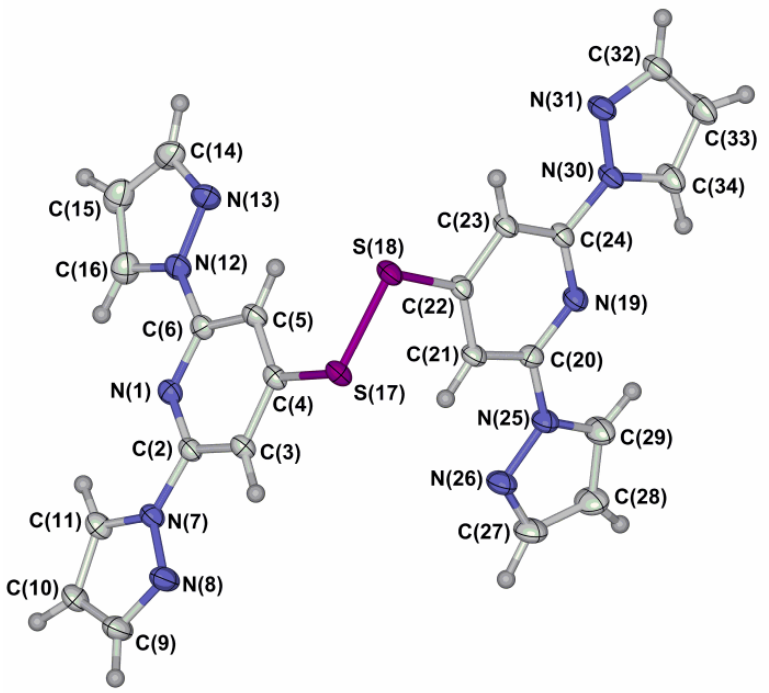

Figure S1. View of the unique molecule in the crystal structure of bppSSbpp, showing the atom numbering scheme employed. Atomic displacement ellipsoids are drawn at the 50 % probability level, except for H atoms which have arbitrary radii.

Colour code: C, white; H, grey; N, blue; S, pink.

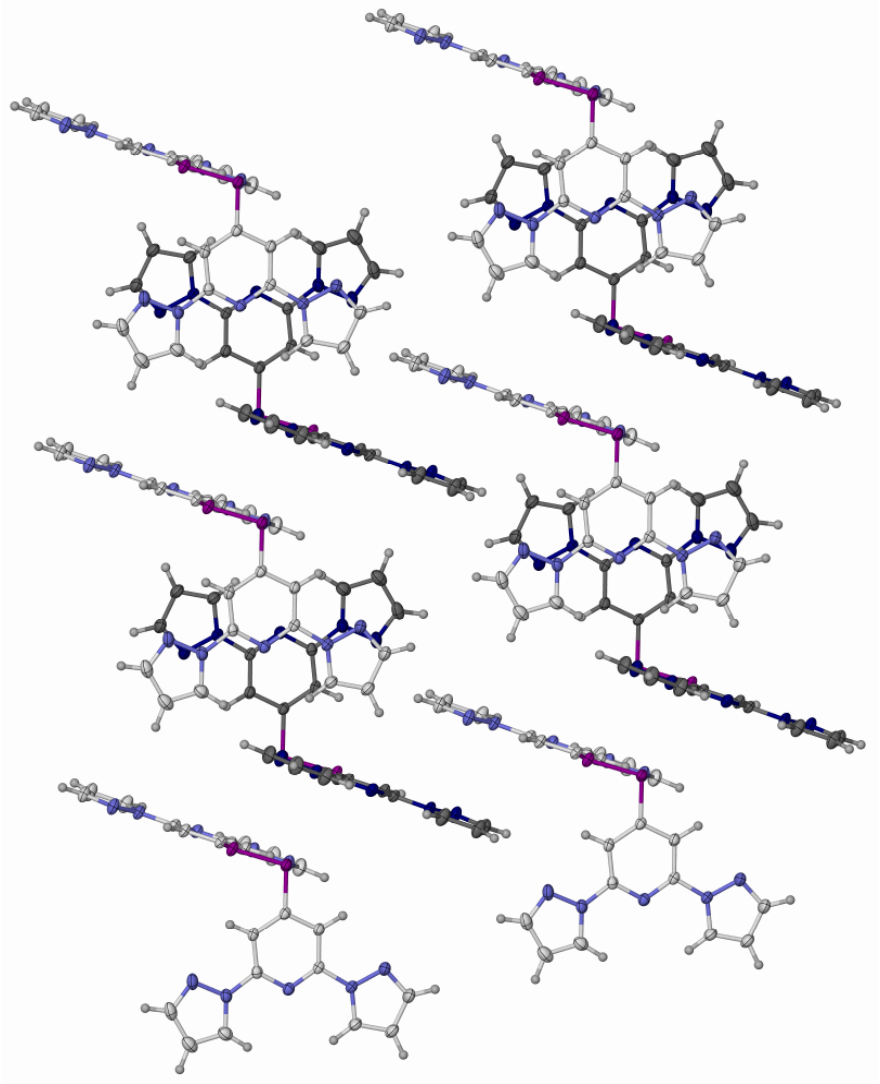

Figure S2. Partial packing diagram of bppSSbpp, showing the intermolecular $\pi\ldots\pi$ interactions in the lattice. Atomic displacement ellipsoids are drawn at the 50 % probability level. Alternate molecules are shown with light and dark colouration, for clarity.

Colour code: C, white or dark grey; H, pale grey; N, pale or dark blue; S, pink.

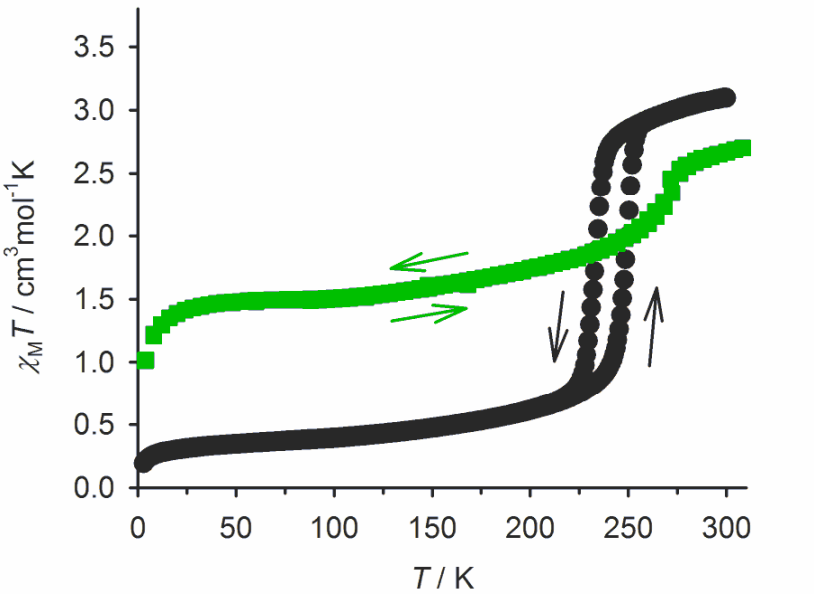

Figure S3. Variable temperature magnetic susceptibility data for the salts of $[Fe(bppSH)_2]^{2+}$: **1[BF$_4$]$_2$** (green) and **1[ClO$_4$]$_2$** (black).

A fully high-spin complex of this type would exhibit $\chi_M T$ = 3.5±0.1 cm^{3}mol^{-1}K.

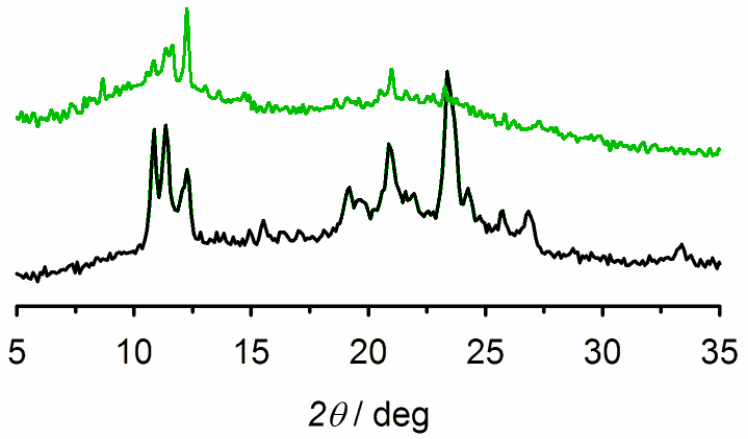

Figure S4. Room temperature X-ray powder diffraction data for the salts of $[Fe(bppSH)_2]^{2+}$: **1[BF$_4$]$_2$** (green, top) and **1[ClO$_4$]$_2$** (black, bottom).

The perchlorate salt **1[ClO$_4$]$_2$** is significantly more crystalline than **1[BF$_4$]$_2$**. That is consistent with their magnetic susceptibility behaviour, since the well-defined spin-transitions in **1[ClO$_4$]$_2$** (major part of the sample) and **1[BF$_4$]$_2$** (minor part of the sample) probably arise from the crystalline fractions of those materials.

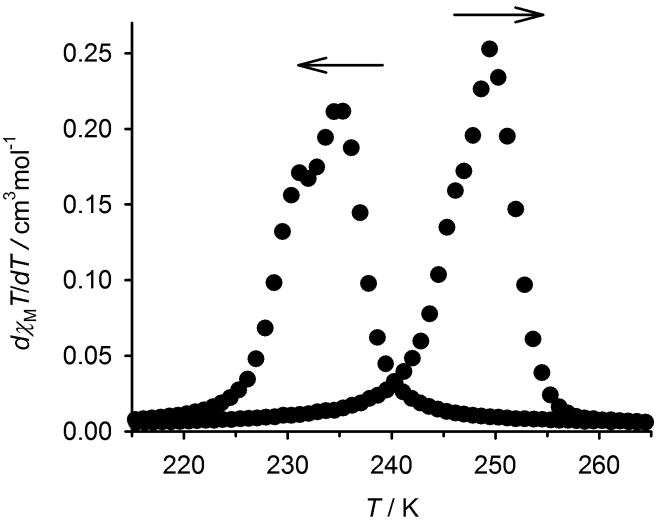

Figure S5. First derivative of the $\chi_M T$ *vs* T curve for **1[ClO$_4$]$_2$** in the vicinity of its abrupt spin-transition (Fig. S3), showing both sides of the hysteresis loop.

The transition in cooling mode is clearly split into two components, with maxima at 231 and 235 K. The warming mode transition also appears to have a low-temperature shoulder, although this is less well resolved.

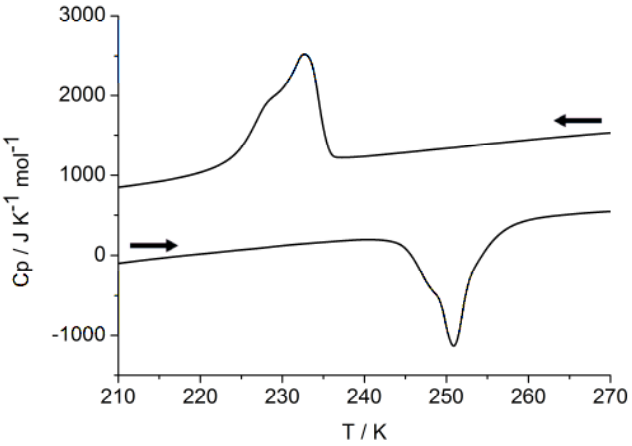

Figure S6. Differential scanning calorimetry (DSC) analysis of **1[ClO$_4$]$_2$**.

The analysis reproduces the hysteretic spin-transition observed in the susceptibility data (Fig. S3), and shows that both sides of the hysteresis loop are split into two components, with approximately equal intensity.

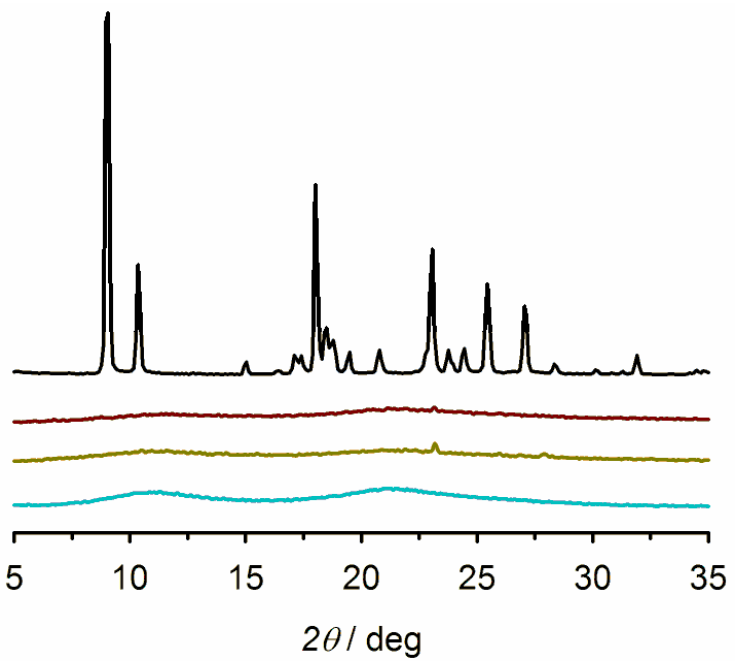

Figure S7. Room temperature X-ray powder diffraction data for bppSSbpp (black) and the complexes **2[BF_4]$_2$** (dark red), **2[ClO_4]$_2$** (yellow) and **3[BF_4]$_2$** (cyan).

The three salts $[M(bppSSbpp)]_nX_{2n}$ compounds are all completely amorphous. The data do confirm that no cocrystallised, uncomplexed bppSSbpp is mixed in with the complex materials, however.

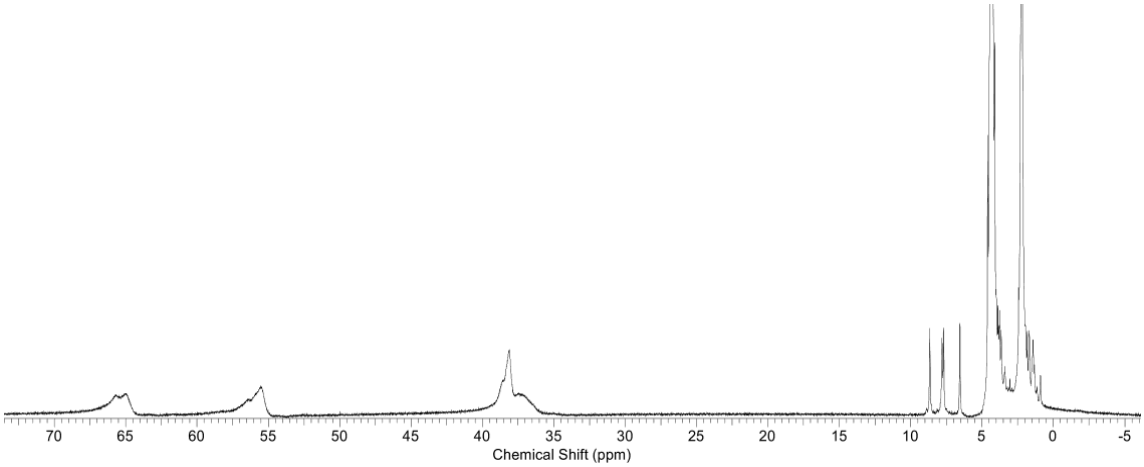

Figure S8. ^{1}H NMR spectrum of **2[BF$_4$]$_2$** in CD_3NO_2.

Each contact-shifted peak is clearly split into two, demonstrating two distinct iron-coordinated environments for the tridentate bpp ligand domain. A metal-free bpp fraction is also visible in the diamagnetic region of the spectrum.

Although the diamagnetic peaks appear intense compared to the contact shifted resonances, the broader linewidth of the paramagnetic peaks reduces their integrals relative to the diamagnetic region. Hence, the relative quantities of free and metal-bound bpp cannot be measured from this spectrum.

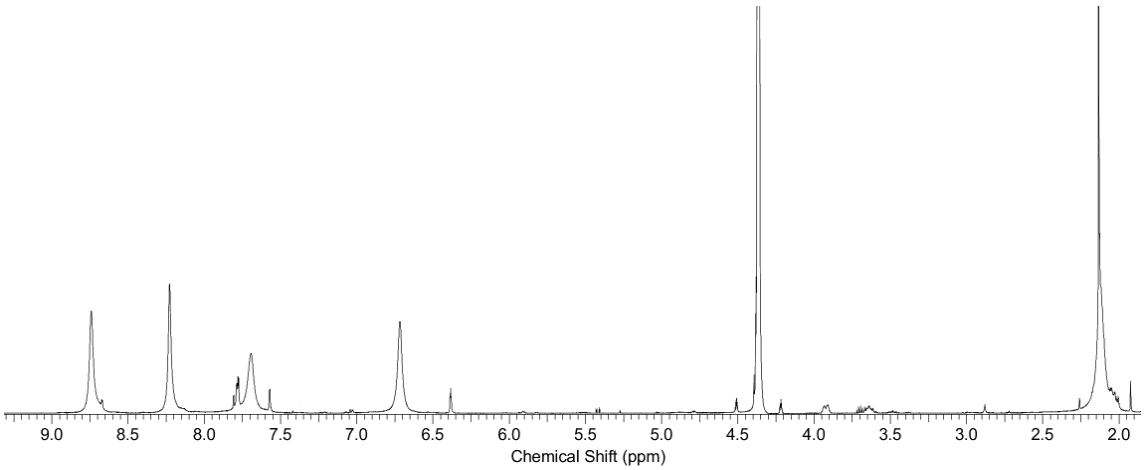

Figure S9. ^{1}H NMR spectrum of **3[BF$_4$]$_2$** in CD_3NO_2.

There are two bpp environments distinguishable in the aromatic part of the spectrum, with an approximate 9:1 integral ratio. The minor environment may correspond to a fraction of uncoordinated bpp residues, based on the peak at 6.38 ppm which has a similar chemical shift to the corresponding peak from the free bppSSbpp ligand (from the pyrazolyl *H*4 proton).

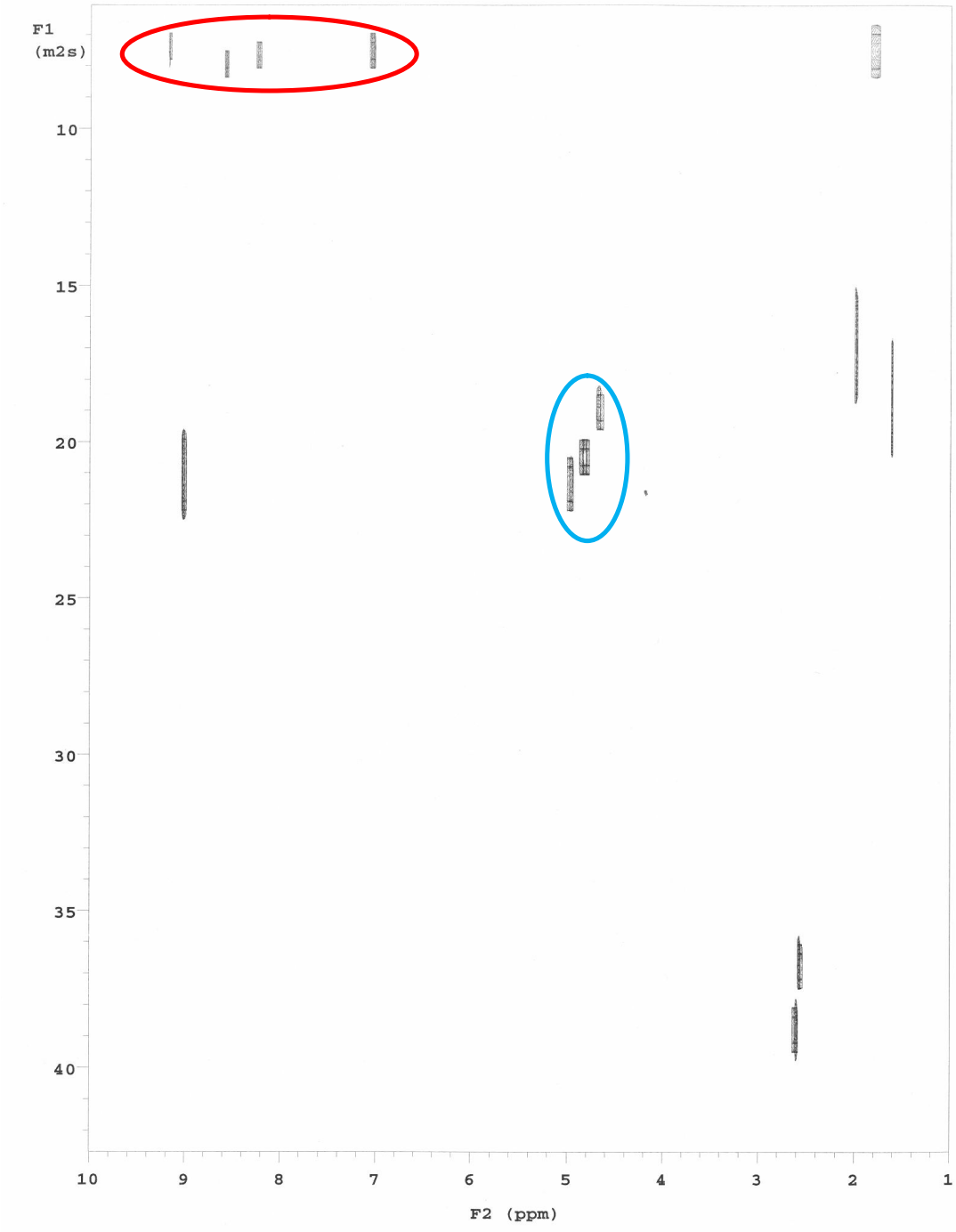

Figure S10. DOSY spectrum of the bppSSbpp ligand in CD_3NO_2.

The red ellipse indicates signals for the ligand, the blue ellipse is the solvent.

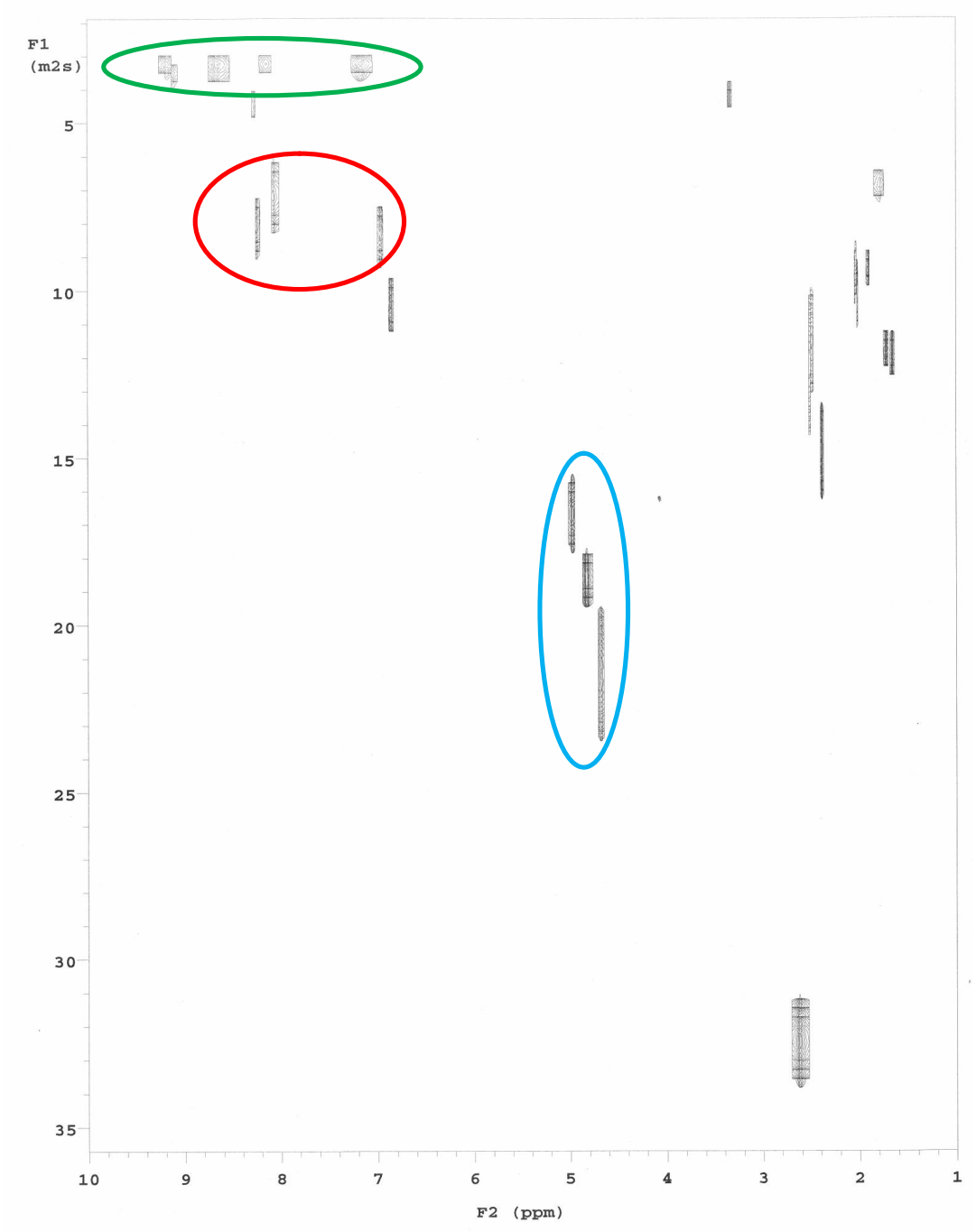

Figure S11. DOSY spectrum of **3[BF_4]$_2$** in CD_3NO_2.

The green ellipse signifies signals from the complex; the red ellipse indicates the free bppSSbpp ligand (Fig. S8); and the blue ellipse is the solvent.

Table S1 Relative intensities and assignments of the principle peaks in the ES mass spectra of the $[\{M(\mu\text{-bppSSbpp})\}_n]^{2n+}$ assemblies (Figs. S10-S12).

The anion content for each molecular ion is shown in brackets. The F^- ions arise from hydrolysis of BF_4^-, and OH^- from deprotonation of water, promoted by the Lewis acidic iron or zinc centres under the conditions of the experiment. In the divalent and trivalent ions derived from the BF_4^- salts, there may be ambiguity about which of F^- or OH^- is actually present.

Assignment	**2[BF_4]$_2$** (M = Fe)		**2[ClO_4]$_2$** (M = Fe)		**3[BF_4]$_2$** (M = Zn)	
	m/*z*	%	*m*/*z*	%	*m*/*z*	%
$[M(bppSSbpp)X]^+$	559.0 (F)	6	639.0 (ClO_4)	6	567.0 (F)	6
$[M(bppSSbpp)_2X]^+$	1043.1 (F)	100	1123.1 (ClO_4)	100	1051.1 (F)	100
$[M_2(bppSSbpp)X_3]^+$	–		892.8 ($[ClO_4]_3$)	17	–	
$[M_2(bppSSbpp)(OH_2)X_3]^+$	–		–		825.1 ($[BF_4]_2F$)	9
$[M_2(bppSSbpp)_2X_3]^+$	1137.1 (F_3), 1205.1 ($[BF_4]F_2$)	44, 7	1297.0 ($[ClO_4]_2OH$), *1378.9 ($[ClO_4]_3$)*[a]	17, *75*[a]	1157.1 (F_3), 1225.1 ($[BF_4]F_2$)	91, 11
$[M_2(bppSSbpp)_3X_2]^{2+}$	869.6 ($[BF_4]_2$)	3	–		879.1 ($[BF_4]_2$)	12
$[M_2(bppSSbpp)_4(OH_2)X_2]^{2+}$	1086.1 ($[BF_4]F$)	7	–		1096.1 ($[BF_4]F$)	3
$[M_2(bppSSbpp)_4(OH_2)_2X_2]^{2+}$	–		1140.9 ($[ClO_4]_2$)	6	–	
$[M_3(bppSSbpp)_3X_4]^{2+}$	–		1010.0	3	–	
$[M_3(bppSSbpp)_4X_4]^{2+}$	–		1210.0 ($[ClO_4]_3OH$)	7	–	
$[M_3(bppSSbpp)_4(OH_2)X_4]^{2+}$	–		–		1182. 1 ($[BF_4]_2F_2$), 1250.9 ($[BF_4]_4$)	4, 4
$[M_3(bppSSbpp)_4(OH_2)_3X_4]^{2+}$	–		–		1200.9 ($[BF_4]_2F_2$), 1266.9 ($[BF_4]_4$)	8, 10
$[M_4(bppSSbpp)_3(OH_2)_3X_6]^{2+}$	–		–		1145.1 ($[BF_4]_6$)	11
$[M_4(bppSSbpp)_4X_6]^{2+}$	1341.1 ($[BF_4]_6$)	16	*1378.9 ($[ClO_4]_6$)*[a]	*75*[a]	1326.1 ($[BF_4]_5F$), 1360.1 ($[BF_4]_6$)	5, 25
$[M_4(bppSSbpp)_4(OH_2)X_6]^{2+}$	–		1306.1 ($[ClO_4]_4[OH]_2$)	5	–	
$[M_4(bppSSbpp)_4X_5]^{3+}$	–		–		855.1 ($[BF_4]_4F$)	7
$[M_5(bppSSbpp)_4X_8]^{2+}$	–		1464.9 ($[ClO_4]_7OH$)	3	–	
$[M_5(bppSSbpp)_4(OH_2)_2X_8]^{2+}$	–		–		1396.0 ($[BF_4]_5F_3$)	5
$[M_5(bppSSbpp)_4X_7]^{3+}$	–		–		912.1 ($[BF_4]_5F_2$)	5
$[M_5(bppSSbpp)_4(OH_2)X_7]^{3+}$	924.1 ($[BF_4]_6F$), 948.0 ($[BF_4]_7$)	3, 3	–		–	
$[M_5(bppSSbpp)_4(OH_2)_3X_7]^{3+}$	–		–		928.0 ($[BF_4]_5[OH]_2$)	6
$[M_5(bppSSbpp)_5X_8]^{2+}$	–		1625.9 ($[ClO_4]_5[OH]_3$), 1748.9 ($[ClO_4]_8$)	2, 3	–	
$[M_6(bppSSbpp)_4X_{10}]^{2+}$	–		1552.8 ($[ClO_4]_8[OH]_2$)	3	–	
$[M_6(bppSSbpp)_4(OH_2)X_{10}]^{2+}$	–		1560.9 ($[ClO_4]_8[OH]_2$)	3	–	

[a]This peak contains a mixture of +1 and +2 charged ions.

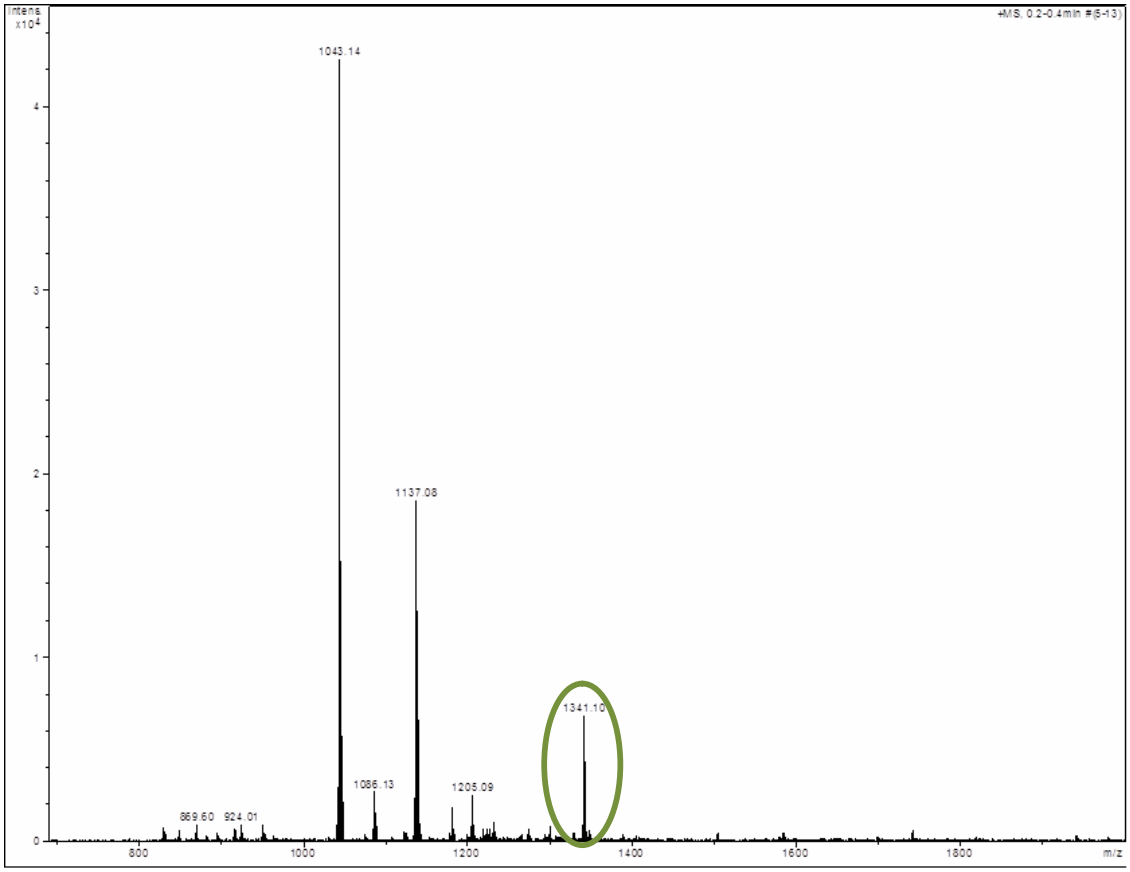

Figure S12. Electrospray mass spectrum of **2[BF_4]$_2$** from $MeNO_2$ solution. Assignments of the peaks are given in Table S1.

The circled peak corresponds to the $[Fe_4(bppSSbpp)_4(BF_4)_6]^{2+}$ ion.

This is the same spectrum shown in Fig. 5 of the main article.

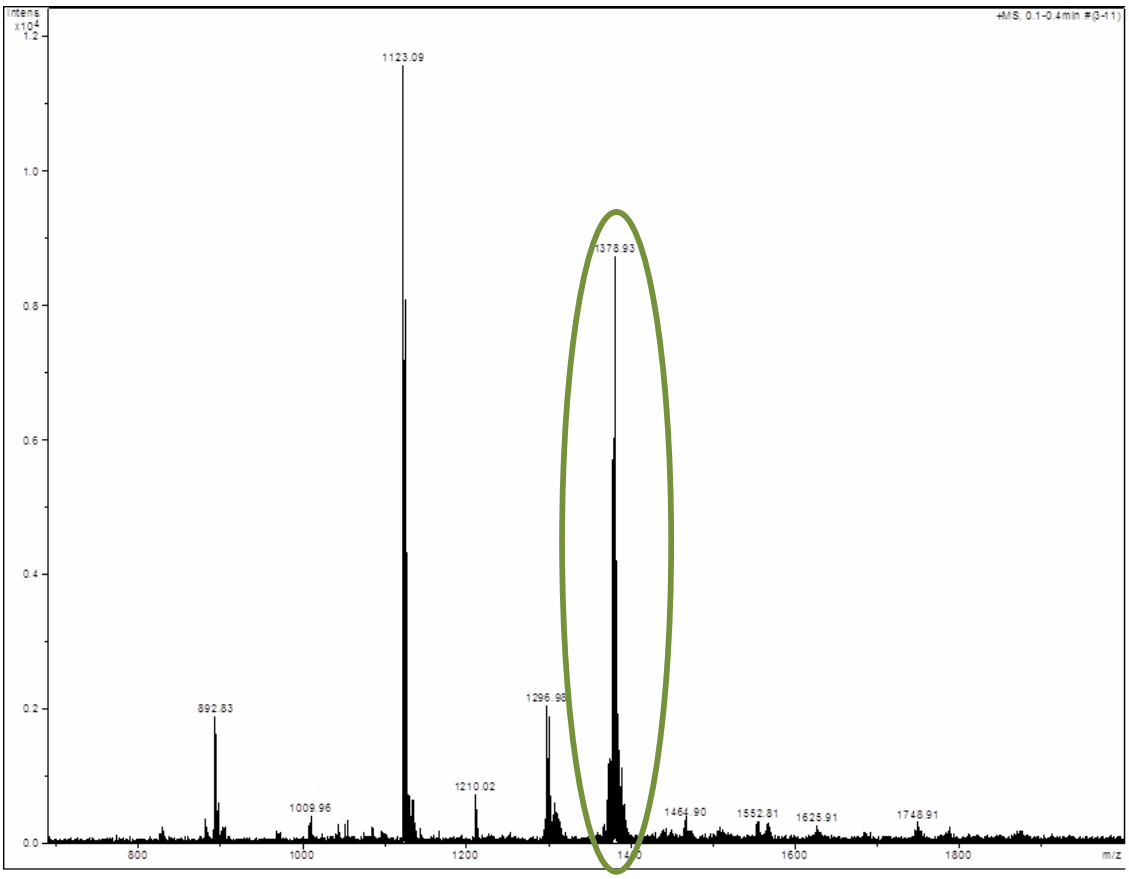

Figure S13. Electrospray mass spectrum of **2[ClO_4]$_2$** from $MeNO_2$ solution. Assignments of the peaks are given in Table S1.

The circled peak is a mixture of +1 and +2 ions, and can be assigned to $[Fe_2(bppSSbpp)_2(ClO_4)_3]^+$ and $[Fe_4(bppSSbpp)_4(ClO_4)_6]^{2+}$.

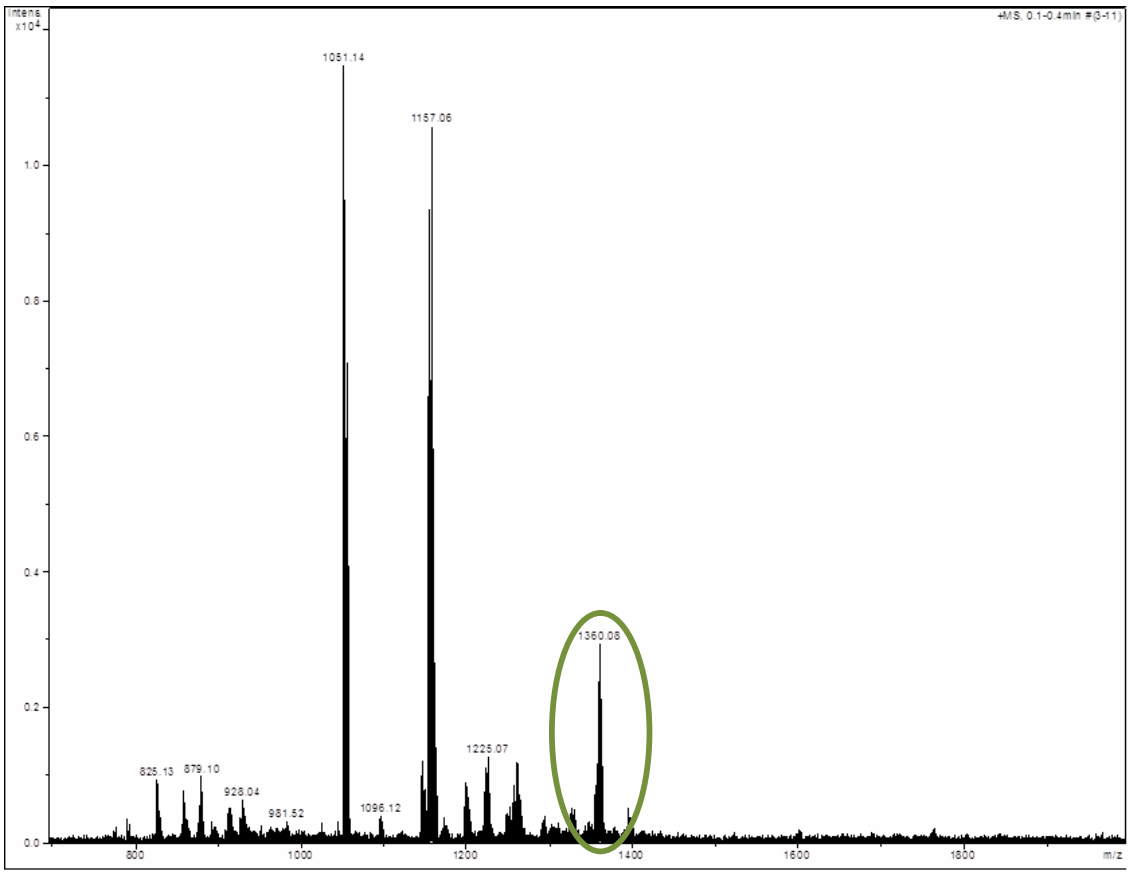

Figure S14. Electrospray mass spectrum of **3[BF_4]$_2$** from $MeNO_2$ solution. Assignments of the peaks are given in Table S1.

The circled peak corresponds to the $[Zn_4(bppSSbpp)_4(BF_4)_6]^{2+}$ ion.